Nuclear Level Densities and Reaction Mechanisms from Inelastic Neutron Scattering*†

DAVID B. THOMSON
Los Alamos Scientific Laboratory, University of California, Los Alamos, New Mexico
(Received 20 September 1962)

The continuous spectrum of fast neutrons scattered inelastically by each of twenty elements has been observed at an incident energy of 7.0 MeV. The elements range in mass number from 26 to 209. The neutron spectra were observed in the range of 0.5 to 4.0 MeV. Similar observations were made for many of the same elements at one or more lower values of incident energy ranging from 4.0 to 6.0 MeV. Angular distributions of the continuous spectra of 5.0 MeV neutrons scattered inelastically by niobium and indium were also measured. The results of the investigation are as follows: (1) Compound-nucleus formation is the predominant reaction mechanism, but direct interaction plays a significant role. (2) The inferred variations of nuclear level density indicate that the nuclear entropy varies with the excitation energy either linearly, as the square root, or in some intermediate fashion, and there is some evidence that the character of this result depends on the shell structure of the nucleus in question. (3) The inferred values of Fermi-gas single-particle level density increase with mass number in the regions between closed shells and go through marked minima near and at closed shells. (4) There is evidence that the effect of pairing is significant at the excitation energies studied.

I. INTRODUCTION

THIS paper is concerned with the measurement of neutron spectra observed in inelastic neutron scattering from medium-weight and heavy nuclei, and with the interpretation of these spectra in terms of nuclear level density variations and nuclear reaction mechanisms. For all but the lightest nuclei, at excitations of several MeV or higher, the level density is usually so high that it may be treated as a continuous function of the excitation energy. The variations of level density with excitation energy and with mass number provide a test of the validity of various nuclear models and are required for a more detailed understanding of a variety of nuclear reactions.

Observation of inelastic neutron scattering is a very useful method for obtaining information concerning nuclear level density variations because over the range of incident energies from less than one-half MeV to greater than 7 MeV, the binary (n,n') reaction predominates and the dominant mechanism is expected to be compound-nucleus formation. If the probing and observed particles are charged, Coulomb-barrier effects considerably restrict the energies and nuclei for which observations of continuous spectra are easily interpretable.

Early measurements of inelastic neutron scattering were made by Graves and Rosen,[1] and O'Neill,[2] for an incident energy of 14 MeV. The results were consistent with the dominance of compound-nucleus processes but the interpretation of these data was complicated by the high probability of second neutron $(n,2n,)$ emission.

Cranberg and Levin[3,4] observed the energy spectrum of neutrons scattered by several heavy elements for incident energies of 2.45, 3.3, and 6.4 MeV and showed that most of the neutrons had a Maxwell-evaporation distribution. These data had the advantage that the incident energy was lower than the threshold for $(n,2n)$ processes, so the interpretation involved only a single temperature. Their data were most accurate at the middle and high side of the peak of the Maxwell-evaporation distribution.

Recent data, taken at incident energies of 5.0 and 7.0 MeV by Ewing and Bonner[5] enabled temperature assignments to be made by assuming the form of the energy distributions. The approximate agreement of their results with direct spectral measurements indicates the usefulness of the Maxwell-evaporation distribution at the middle and low side of the peak.

Spectral data taken earlier with other reactions have also been fruitful. Spectra from (p,n) reactions,[6] (p,p') reactions,[7,8] and (α,α') reactions,[9] have indicated the general usefulness of the Maxwell-evaporation distribution, the frequent applicability of the Fermi-gas model, and a contribution of direct interactions to the excitation of the lower lying states.

More complicated reactions, such as the fission neutron spectrum studied by Terrell,[10,11] and heavy ion

* Work done under the auspices of the U. S. Atomic Energy Commission.

† The major portion of this work, including all the observed spectra, was submitted as a thesis in partial fulfillment of the requirements for a PhD degree at the University of Kansas, 1960. (Thesis available from University Microfilms, Inc., 313 N. First Street, Ann Arbor, Michigan; L.C. Card No. MIC 61-287.)

[1] E. R. Graves and L. Rosen, Phys. Rev. **89**, 343 (1953).

[2] G. K. O'Neill, Phys. Rev. **95**, 1235 (1954).

[3] L. Cranberg and J. S. Levin, Phys. Rev. **103**, 343 (1956).

[4] L. Cranberg and J. S. Levin, *Proceedings of the Conference on Neutron Physics by Time-of-Flight, Gatlinburg, Tennessee, 1956* [Oak Ridge National Laboratory ORNL-2309 (unpublished)], p. 84.

[5] R. Ewing, thesis, The Rice Institute, Houston, Texas, 1959 (unpublished). R. Ewing and T. W. Bonner (private communication).

[6] P. C. Gugelot, Phys. Rev. **81**, 51 (1951).

[7] P. C. Gugelot, Phys. Rev. **93**, 425 (1954).

[8] B. L. Cohen and A. G. Rubin, Phys. Rev. **113**, 579 (1959).

[9] N. O. Lassen and N. O. Roy Poulsen, *Comptes Rendus du Congrès International de Physique Nucléaire, Paris, 1958* (Dunod, Paris, 1959).

[10] J. Terrell, Phys. Rev. **113**, 527 (1959).

[11] J. Terrell (private communication).

experiments[12,13] have indicated[14] the wide applicability of the statistical treatment of nuclear properties, as have very high (BeV) energy bombardments.[15] Determination of nuclear level density variations from these experiments is less direct, however, than for the case where one binary process such as (n,n') dominates. Clearly, however, the charged-particle data are invaluable where they can be obtained since a sound treatment of the data must yield a result for the nuclear level density function which is independent of the probing particle and its energy.

The foregoing discussion has illustrated some of the nuclear processes to which the thermodynamic treatment of nuclear level density is applicable. There are many gaps in the available systematic information, however. The need for much more data taken over as wide a range of mass number and excitation energy as possible furnished the incentive for the investigation reported here.

II. THEORY

We now consider the simple binary process of inelastic neutron scattering initiated by a beam of monoenergetic neutrons incident on a specific target nucleus, under conditions such that the excitation energies of the residual nucleus may be treated as a continuum.[16,17]

A. Fundamental Relations

Let E_0 be the energy of the incident neutron, E the energy of the inelastically scattered neutron, and E^* the excitation energy of the excited residual nucleus, all these energies being in the center-of-mass system. Assuming, for heavy target nuclei, that all of the kinetic energy of the reaction products is carried by the neutron, we have

$$E_0=E+E^*. \tag{1}$$

From the reciprocity theorem,[18,19]

$$N(E)=\text{const}EW(E^*)\sigma_i(E,E^*). \tag{2}$$

$N(E)$ is the energy distribution of the inelastically scattered neutrons for a fixed E_0, $W(E^*)$ is the level density of the excited residual nucleus, and $\sigma_i(E,E^*)$ is the inverse cross section. Equation (2) may not require the special assumption of compound-nucleus (CN) formation but is usually derived for this case. When the CN assumption is made, σ_i is essentially the cross section for the formation of the compound nucleus by the emergent neutron and the excited residual nucleus.

One may relate the nuclear level density to the nuclear entropy by the relation

$$W(E^*)=\exp S(E^*). \tag{3}$$

The well-known Taylor series expansion of $S(E^*)$, together with Eq. (2), then yields

$$\ln[N(E)/E]=-E/T+\ln \text{ const} \tag{4}$$

when the assumption is made that $\sigma_i(E,E^*)$ is constant with energy.

Equation (4) is the familiar[18,19] Maxwell-evaporation spectrum, where T is the nuclear temperature, and is given by the slope of a plot of $\ln[N(E)/E]$ vs E. If $\partial S(E^*)/\partial E^*$ is sufficiently slowly varying over the range of E^* considered, T will be a constant for any given spectrum. In general, the nuclear temperature is a function of E^*.

B. Predictions of Level Density Variations from Nuclear Models

The general form of the energy distribution given by Eq. (4) is not dependent on a particular nuclear model. However, the specific values of the nuclear temperature provide a criterion for testing various models which are appropriate to the statistical description of the excited states of nuclei.

One may infer from a model an expression for the equation of state

$$E^*=E^*(T), \tag{5}$$

and then calculate the entropy from the expression

$$S(E^*)=\int\frac{dE^*}{T(E^*)}. \tag{6}$$

The formal relation

$$\partial S/\partial E^*=1/T(E^*), \tag{7}$$

defines a temperature which is, in general, dependent on E^*. The equation of state (5) may be obtained from a statistical treatment of nuclear systems. From this viewpoint Bethe[16] and others have developed statistical treatments of nuclear level densities on the basis of such widely differing assumptions as those of the Fermi-gas model and the liquid-drop model. The Fermi-gas model is a special case of the independent-particle model of the nucleus which in turn has been strongly supported by the success of the optical model[20] in predicting nuclear reaction cross sections, and the shell model[21] in predicting properties of the ground and low-lying nuclear states. The Fermi-gas model, as treated by Mayer and Mayer,[22] yields an equation of state of the

[12] C. D. Goodman and J. N. Need, Phys. Rev. **110**, 676 (1958).
[13] A. Zucker, Nucl. Phys. **6**, 420 (1958).
[14] K. J. LeCouteur and D. W. Lang, Nucl. Phys. **13**, 32 (1959).
[15] S. Katcoff, Phys. Rev. **114**, 905 (1959).
[16] H. A. Bethe, Rev. Mod. Phys. **9**, 69 (1937).
[17] V. F. Weisskopf, Phys. Rev. **52**, 295 (1937).
[18] J. M. Blatt and V. F. Weisskopf, *Theoretical Nuclear Physics* (John Wiley & Sons, Inc., New York, 1952).
[19] H. A. Bethe and P. Morrison, *Elementary Nuclear Theory* (John Wiley & Sons, Inc., New York, 1956), 2nd ed.
[20] H. Feshbach, C. E. Porter, and V. F. Weisskopf, Phys. Rev. **96**, 448 (1954).
[21] M. G. Mayer and J. H. D. Jensen, *Elementary Theory of Nuclear Shell Structure* (John Wiley & Sons, Inc., New York, 1955).
[22] J. E. Mayer and M. G. Mayer, *Statistical Mechanics* (John Wiley & Sons, Inc., New York, 1940).

form

$$E^* = aT^2, \tag{8}$$

where a is proportional to the single-particle level spacing at the top of the Fermi sea. The quantity a has been estimated[10] to be $a = A/10$ for nuclei. Equation (8) leads to a level density expression of the form

$$W(E^*) = \text{const} e^{2(aE^*)^{1/2}}. \tag{9}$$

More detailed treatments[16,23,24] lead to expressions of the form

$$W(E^*) = \text{const} f(E^*) e^{2(aE^*)^{1/2}}. \tag{10}$$

C. Shell Model and Odd-Even Effects

The idea that nucleons are confined to certain well-defined orbits, or shells, implies that departures from the prediction of the pure Fermi gas might be expected. Newton[24] has considered the effects of shell structure in an attempt to fit level spacings observed for many nuclei by the slow-neutron resonance method. He uses an expression of the form

$$G = \text{a}(\vec{j}_N + \vec{j}_Z + 1)A^{2/3}, \tag{11}$$

for the sum of the neutron and proton single-particle level densities. The $\vec{j}_N$ and $\vec{j}_Z$ are defined as effective values of the neutron and proton angular momenta in the outermost shell and are assigned values corresponding to a spherical potential for shells in the immediate neighborhood of magic numbers, and a constant value in the regions in between. Newton's evaluation of Eq. (11) shows significant dips in the level density near closed shells, and approximate agreement with Fermi-gas predictions in the regions between closed shells.

In analyzing much of the hitherto reported experimental spectral data, LeCouteur and Lang[14] have noted a general agreement of nuclear level densities, at excitations of 5 to 10 MeV and higher, with Fermi-gas predictions and have also noted observable departures from these predictions presumably due to shell effects.

It is well known that nuclear level densities are strongly correlated with the odd-even character of the nucleus. This effect is usually taken account of[25,26] by assuming that nuclear pairing depresses the ground state of a nucleus. The zero level of excitation is adjusted to compensate for this effect. One should look therefore, for the effects of pairing energy, as well as of shell effects, in any systematic study of nuclear level densities.

D. Effects of Nuclear Reaction Mechanisms

The correct interpretation of continuous spectra in terms of the true level density requires knowledge of the variation with energy of the inverse cross section $\sigma_i(E,E^*)$, Eq. (2), making it necessary to discuss the most likely types of reaction mechanisms and their possible effects on $\sigma_i(E,E^*)$. Let us write

$$\sigma_i(E,E^*) = \sigma_i^{\text{CN}}(E,E^*) + \sigma_i^{\text{DI}}(E,E^*), \tag{12}$$

where the superscripts CN and DI refer, respectively, to the compound-nucleus and direct-interaction mechanisms. Equation (12) assumes that there are no interference effects between the two terms. Experimental evidence has indicated that both mechanisms are involved and must be considered.

The compound-nucleus description and the related statistical assumption have been reviewed by many authors.[18,19,27,28] The calculations of Hauser and Feshbach[28,29] for inelastic neutron scattering where many levels are involved predict isotropic angular distributions. Experiments such as those of Rosen and Stewart[30] for 14-MeV incident neutrons, and Cranberg and Levin[3,4] at several MeV, indicate that 80 to 90% of the observed neutrons give an isotropic, or near isotropic, angular distribution, for the case of continuous spectra.

The direct interaction mechanism for inelastic neutron scattering, suggested by the success of the optical model,[19,20] has been studied by many authors, including Butler,[31] Lamarsh and Feshbach,[32] Yoshida,[33] and Glendenning.[34,35] It has been predicted that direct interactions should be characterized by small energy loss[35] of the incident particle and by sharp variations in the angular distributions, frequently with strong forward peaking.[27,36] The inelastic neutron scattering experiments of Rosen and Stewart[30] show strong forward peaking for those neutrons for which the energy transfer is the smallest, and isotropy for those neutrons for which the energy transfer has large values. The inelastic scattering of protons,[37,38] and other charged effects of direct interactions.

The present work represented an attempt experimentally to observe the effect of the inverse cross section on the spectra and to get a more accurate description than had previously been obtained, of the particles,[9,39] has generally enabled one to observe the

[23] J. M. B. Lang and K. J. LeCouteur, Proc. Phys. Soc. (London), **67**, 586 (1954).
[24] T. D. Newton, Can. J. Phys. **34**, 804 (1956).
[25] H. Hurwitz, Jr. and H. A. Bethe, Phys. Rev. **81**, 898 (1951).
[26] T. Ericson, *Advances in Physics*, edited by N. F. Mott (Taylor and Francis, Ltd., London, 1960), Vol. 9, p. 425.
[27] D. C. Peaslee, Ann. Rev. Nucl. Sci. **5**, 99 (1955).
[28] W. Hauser and H. Feshbach, Phys. Rev. **87**, 366 (1952).
[29] Remarks by H. Feshbach, Brookhaven National Laboratory Report. BNL-331 (unpublished), p. 59.
[30] L. Rosen and L. Stewart, Phys. Rev. **107**, 824 (1957).
[31] S. T. Butler and O. H. Hittmein, *Nuclear Stripping Reactions* (John Wiley & Sons, Inc., New York, 1957).
[32] J. R. Lamarsh and H. Feshbach, Phys. Rev. **104**, 1633 (1956).
[33] S. Yoshida, Progr. Theoret. Phys. Japan, **19**, 169 (1958).
[34] N. K. Glendenning, thesis, University of Indiana, 1958 (unpublished). N. K. Glendenning and K. Ford (private communication).
[35] N. K. Glendenning, Phys. Rev. **114**, 1297 (1959).
[36] N. Austern, S. T. Butler, and H. McManus, Phys. Rev. **92**, 350 (1953).
[37] R. D. Sharp and W. W. Buechner, Phys. Rev. **112**, 897 (1958).
[38] F. D. Seward, Phys. Rev. **114**, 514 (1959).
[39] G. B. Shook, Phys. Rev. **114**, 310 (1959).

variation of nuclear level density with E^* and with mass number in the range of several MeV excitation.

III. PROCEDURE

Extensive pioneer work[3,4,40,41] was done in Los Alamos by Cranberg, Levin, and associates in developing the neutron time-of-flight technique into a very useful system for neutron spectroscopy in the MeV region. This system will be referred to as the Los Alamos time-of-flight system, and represents the basic experimental method used.

A. The Los Alamos Time-of-Flight System

The Los Alamos large Van de Graaff accelerator[42] is used with the $T(p,n)He^3$ and $D(d,n)He^3$ reactions to produce monoenergetic neutrons of energies up to about 8 MeV. Energy spread is caused primarily by the thickness of the gas targets, with a minor contribution due to straggling of the charged-particle beam in the Ni window. A comparison of the time spectra for gas-in and gas-out runs is used to verify that essentially all of the neutrons are being produced by the source reaction at the desired energy.

A portion[43] of the present work was accomplished with the beam-pulsing system previously described[3,4,40,41] where the charged-particle beam was deflected, or "chopped," after acceleration. For later work, apparatus developed by McKibben and associates[44] was used which consisted of a radio-frequency electrostatic beam deflector (called the chopper) in the high-voltage terminal of the accelerator.

For this work, the chopper was operated at a frequency of 2.0 Mc with two bursts per rf cycle. A typical current on target was 2.0 μA at a burst half-width of about 8 mμsec, a burst occurring once very quarter μsec.

The proton-recoil neutron-detector was a plastic scintillator, (Nuclear Enterprises, Ltd., NE 102) of length $1\frac{1}{2}$ in. and diameter of $1\frac{3}{4}$ in. The plastic was canned with a magnesium-oxide reflector by the Harshaw Chemical Co., and was mounted on a 6810A photomultiplier. Figure 1 shows a diagram of the detector and shield arrangement used.

Neutron scattering is observed by placing the scattering sample two or three inches from the neutron source at 0° to the accelerator beam and then aiming the collimator directly at the sample, as shown in Fig. 1. A typical scattering sample consisted of a hollow cylinder 2-in. long, about 0.75-in. o.d. and 0.375 in. i.d. These dimensions optimize considerations[45] of counting rate, multiple scattering, and subtended source energy spread.

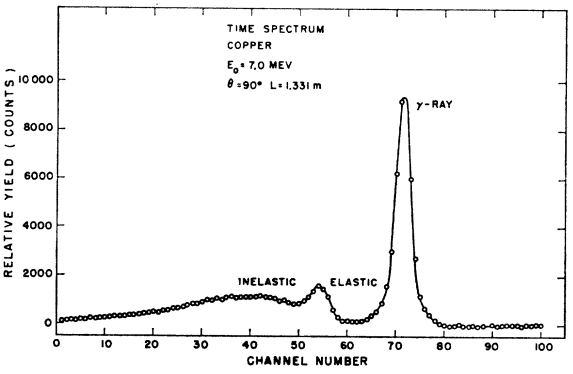

FIG. 2. Time spectrum showing the scattering of 7.0-MeV neutrons by copper (background not subtracted).

Neutron energies were determined by straightforward measurement of the time required for the neutrons to travel a prescribed flight path. The pulsed-beam reference pulse was derived by electrostatic induction from a cylinder through which the beam passes. The pulse produced by the arrival of a fast neutron at the detector was taken directly from the last dynode of the 6810A photomultiplier. The time-to-pulse-height converter has been discussed in considerable detail previously.[46] The output of the converter was amplified and presented on a 100-channel pulse-height analyzer, as in the earlier work.[3,4,46]

Figure 2 shows a typical time spectrum for the arrangement as it was used in the later stages of the investigation. This spectrum is for 7-MeV neutrons scattered by copper, with the detector set at 90°. The neutron detector also detects the prompt gamma rays resulting from the inelastic scattering. The gamma-ray line is used to determine a reference point for the

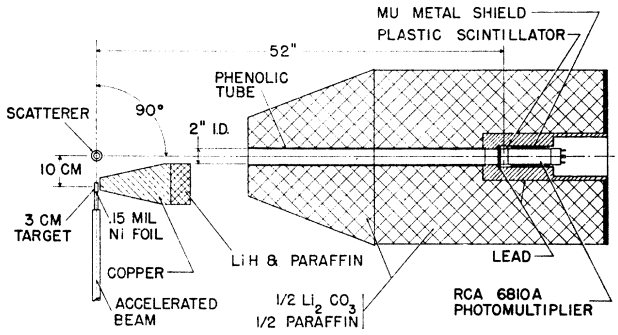

FIG. 1. The scattering geometry.

[40] L. Cranberg, *Proceedings of the International Conference on the Peaceful Uses of Atomic Energy, Geneva, 1955* (United Nations, New York, 1956), Vol. 4, Paper P/577.
[41] L. Cranberg, R. K. Beauchamp, and J. S. Levin, Rev. Sci. Instr. 28, 89 (1957).
[42] J. L. McKibben, Atomic Energy Commission Report 2038, 1948 (unpublished).
[43] D. B. Thomson and L. Cranberg, Bull. Am. Phys. Soc. 4, No. 4, Paper NA-12 (1959).
[44] J. L. McKibben, Los Alamos Internal Reports, 1959 (unpublished).
[45] L. Cranberg and J. S. Levin, Los Alamos Report 2177, 1959 (unpublished).
[46] W. Weber, C. W. Johnstone, and L. Cranberg, Rev. Sci. Instr. 27, 166 (1956).

neutron flight time since it represents a readily identifiable structure. Because it is desired that the detector sensitivity be as stable as possible, the 100-channel analyzer was gated by a "slow" system as in the previous work.[3,4,46] The anode output of the photomultiplier was amplified by a stable slow amplifier (Los Alamos model 101, and associated preamp) and fed to a Los Alamos model 750 scaler whose output gave the desired gate. Thus the discriminator bias which determines the detector sensitivity was dependent on a relatively stable electronic system.

As in earlier work[3,4] two essential calibrations are required; the time per channel and the energy sensitivity of the detector. The time per channel was obtained by setting the detector angle at zero degrees, observing a monoenergetic group of neutrons of known velocity, changing the flight path and observing the number of channels on the time spectrum that the neutron peak moves. A plot of flight path vs channel number gives the desired calibration curve, which was linear over the spectrum within about 2%.

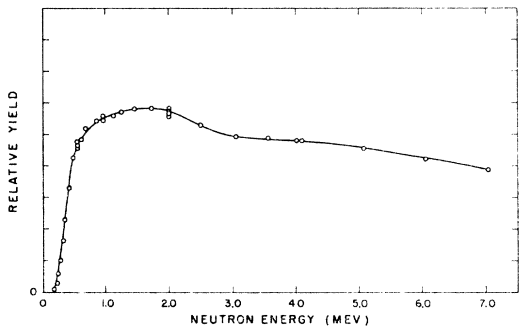

FIG. 3. Relative detector sensitivity as a function of neutron energy.

The energy sensitivity of the detector is needed to obtain a true spectrum from an observed spectrum such as Fig. 2. The detector sensitivity was obtained by observing the known zero-degree yield of a source of monoenergetic neutrons as a function of neutron energy. For this purpose, the $T(p,n)He^3$ reaction[47] was used for neutron energies of about 200 keV to 5.0 MeV, and the $D(d,n)He^3$ yield[48] was used for neutron energies in the range of 4 to 8 MeV. Figure 3 shows a typical detector sensitivity curve.

The following method was found useful for setting the detector bias in a reproducible manner. Figure 4 shows a typical slow system pulse-height spectrum for the 60-keV gamma rays from an Am^{241} source. Also shown is the pulse-height spectrum, taken under identical conditions, for 0.56-MeV neutrons produced by the accelerator. It is seen that the Am^{241} produces a characteristic peak at about the same pulse heights as are produced by neutrons of energies near the steep portion of the detector sensitivity curve. By setting the slow discriminator to a desired point relative to the peak or some other characteristic feature of the americium pulse-height distribution, one can compensate for day to day drifts of gain of the photomultiplier and the slow system. Figure 3, for example, corresponds to a discriminator setting of one-half the americium peak value.

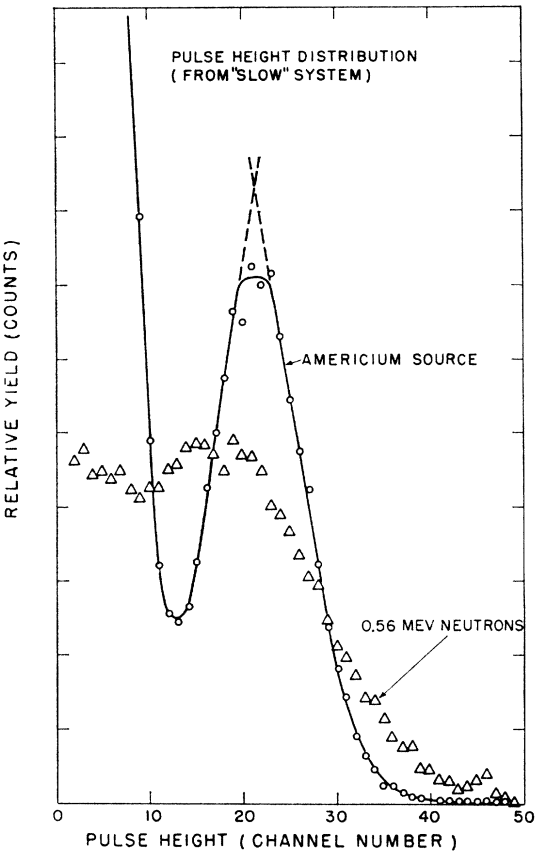

FIG. 4. Pulse-height distributions from the "slow" system amplifier for the Am^{241} source and for 0.56-MeV neutrons.

B. Choice of Elements and Experimental Parameters

Previous measurements[2,3,4,30] indicated that observations taken at 90°, where the background and elastic scattering are small, would give spectral results fairly typical of those at any angle, so that most of the data were taken at 90°.

The characteristics of the particular arrangement used for the measurements allowed accurate observation of the spectrum of the inelastically scattered neutrons in the energy range from one-half to three or four MeV, for any given scattering sample. The lower limit of the spectrum was determined by the detector sensitivity cutoff and by poor statistics in that region of the spec-

[47] Summary by J. E. Perry and E. Haddad (private communication).

[48] Summary by R. K. Smith, J. E. Perry, and R. L. Henkel (private communication).

trum. The upper limit was determined by the time resolution and the ability to distinguish inelastic neutrons from the elastic peak. Typical values of the parameters were as follows: flight path about 1.5 m, time resolution eight mμsec full width at half-maximum, pulsed-beam repetition rate 4 Mc, and detector sensitivity cutoff at about one-half MeV. These parameters represented a compromise among the various factors which affect intensity and resolution, and were picked to optimize both the counting rate and the range of E^* values observed. These parameters give an observed spectrum that is most accurate for those energies in the vicinity of the average excitation energy (E_0-2T).

A maximum incident energy of 7 MeV was chosen because it is the highest neutron energy obtainable before three-body breakup[49] competes with the $D(d,n)He^3$ reaction causing a complicating lower energy group of source neutrons. In addition, at incident neutron energies not much higher than 7 MeV, $(n,2n)$ processes become significant and complicate interpretation of the spectra.

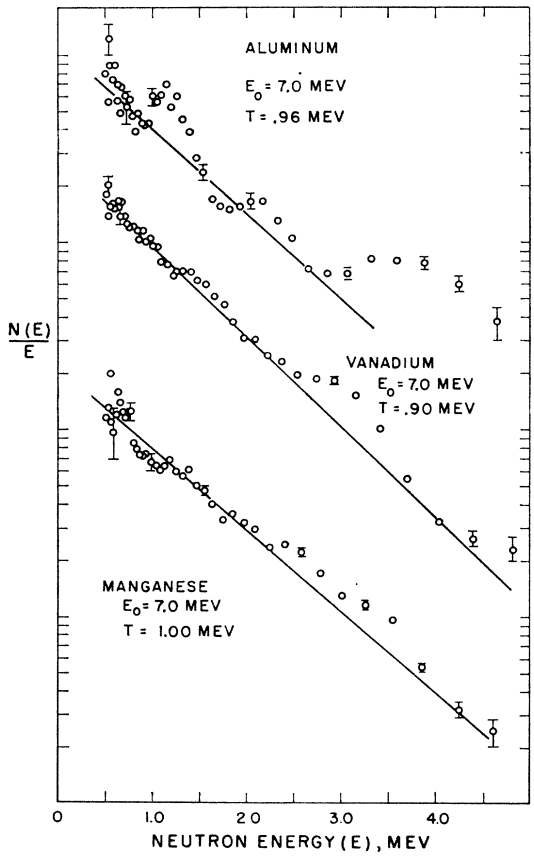

FIG. 5. Plots of $\ln[N(E)/E]$ vs emitted neutron energy (E) for 7.0-MeV neutrons scattered inelastically by aluminum, vanadium, and manganese.

[49] L. Cranberg, A. H. Armstrong, and R. L. Henkel, Phys. Rev. **104**, 1639 (1956).

With these considerations in mind, continuous spectra were observed for twenty elements at 7 MeV. The elements were chosen to cover as wide a range of mass number as possible. The lower limit to the mass number was determined by the appearance of marked structure in the observed spectra. The upper limit was imposed by the complications associated with fission. An attempt was made to pick elements corresponding to both peaks and valleys of Newton's[24] Fig. 5. Most of the nuclides were of the odd-even species with only one or two predominant isotopes.

For eleven of these elements observations were made at more than one incident energy to get information as to the variation of level density with E^*. The lowest incident neutron energy used was 4.0 MeV, where the yield of the $T(p,n)He^3$ reaction is quite high, and where the E^* values involved are still large enough for the spectra to appear as a continuum for many nuclei. Three elements, indium, niobium, and thallium, were studied in greater detail since they illustrated the various kinds of results that were obtained for the other elements. Their spectra were observed for each of the following incident energies: 4.0, 5.0, 6.0, and 7.0 MeV. This procedure made possible an interesting "overlap"

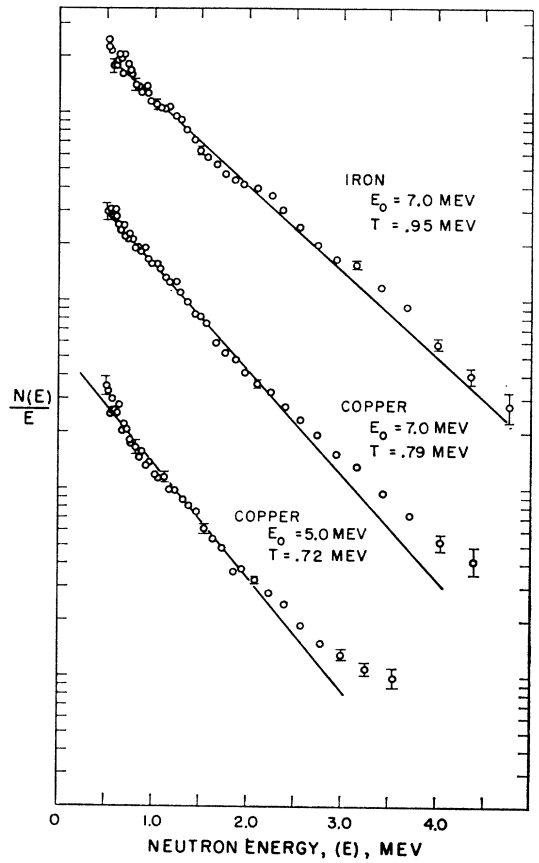

FIG. 6. Plots of $\ln[N(E)/E]$ vs emitted neutron energy (E) for 7.0-MeV neutrons scattered inelastically by iron and copper, and for 5.0-MeV neutrons scattered by copper.

analysis (Discussion of Results) which hopefully leads to a separation of the effects of $S(E^*)$ and $\sigma_i(E,E^*)$.

Several independent temperature measurements were made for each element and incident energy studied. Figures 5 through 10 show typical results. Each temperature slope drawn represents an average of all the results obtained for a given element and incident energy. Table I lists the neutron source characteristics for each of the incident neutron energies chosen for the work. Figure 10 shows typical energy resolution functions. The triangles show the effect of both the target thickness and the time width of the pulsed beam.

C. Treatment of the Spectral Data

Neutron spectra were obtained from the raw data in a straightforward manner as in previous work.[3,4,50] For a given observation, the time spectrum was obtained by subtracting a sample-out run from the sample-in run, and correcting for a small residual nonsynchronous background (due, for example, to activation of the sample). Counts corresponding to elastically scattered neutrons were subtracted by fitting an appropriate monoenergetic neutron line shape to the elastic peak of the time spectrum. It was found that the spectrum for indium at 4.0 MeV gave a strong elastic peak at forward angles which agreed in shape with the gamma-ray peak within a few percent for each channel having an amplitude of 5% or more of the peak channel. This agreement was primarily due to the fact that the beam-pulse duration provided the dominant contribution to the linewidth. Furthermore Fig. 11 shows a comparison, at

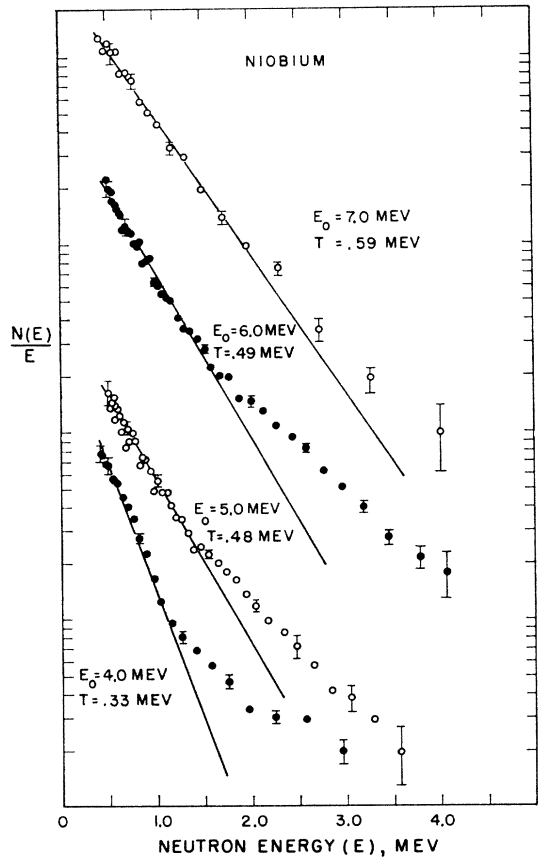

FIG. 7. Plots of $\ln[N(E)/E]$ vs emitted neutron energy (E) for the inelastic scattering of neutrons by niobium at incident energies of 4.0, 5.0, 6.0, and 7.0 MeV.

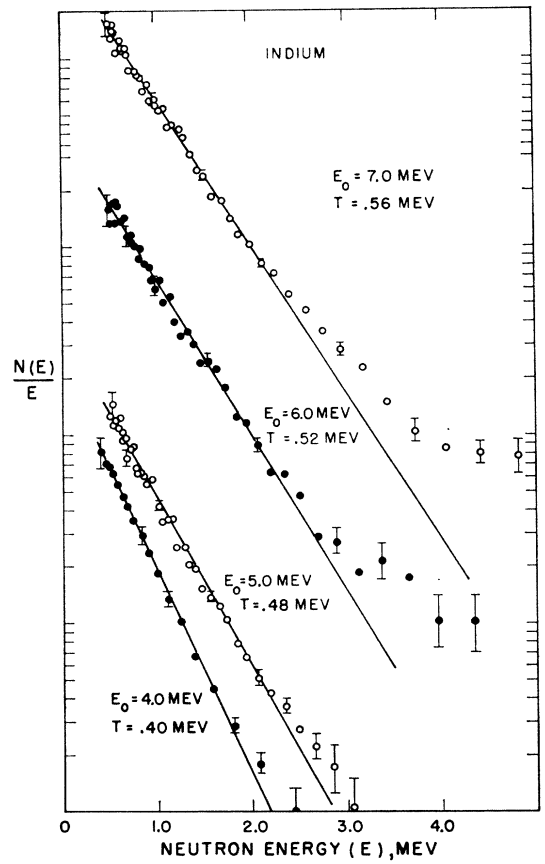

FIG. 8. Plots of $\ln[N(E)/E]$ vs emitted neutron energy (E) for the inelastic scattering of neutrons by indium at incident energies of 4.0, 5.0, 6.0, and 7.0 MeV.

TABLE I. Incident beam operating conditions.[a]

Neutron energy (E_0) (MeV)	Reaction	Accelerator energy (MeV)	Loss in Ni foil (keV)	Target thickness (keV)
4.00	$T(p,n)He^3$	4.961	148	76.8
5.00	$D(d,n)He^3$	2.318	399	288
6.00	$D(d,n)He^3$	3.162	323	206
7.00	$D(d,n)He^3$	4.084	269	160

[a] The targets consist of 2 atm of tritium (or deuterium) gas in a 3-cm length target chamber. The foil is nickel and of thickness 0.150 mil (3.30 ± 0.03 mg/cm^2). The energy losses in the gas targets and in the nickel foil were obtained from curves compiled by J. E. Perry and R. K. Smith, L.A.S.L. (1954). These values have been checked from time to time by various members of the Los Alamos large Van de Graaff accelerator group.

[50] L. Cranberg, R. B. Day, L. Rosen, R. F. Taschek, and M. Walt, Progr. Nucl. Energy **1**, 107 (1956).

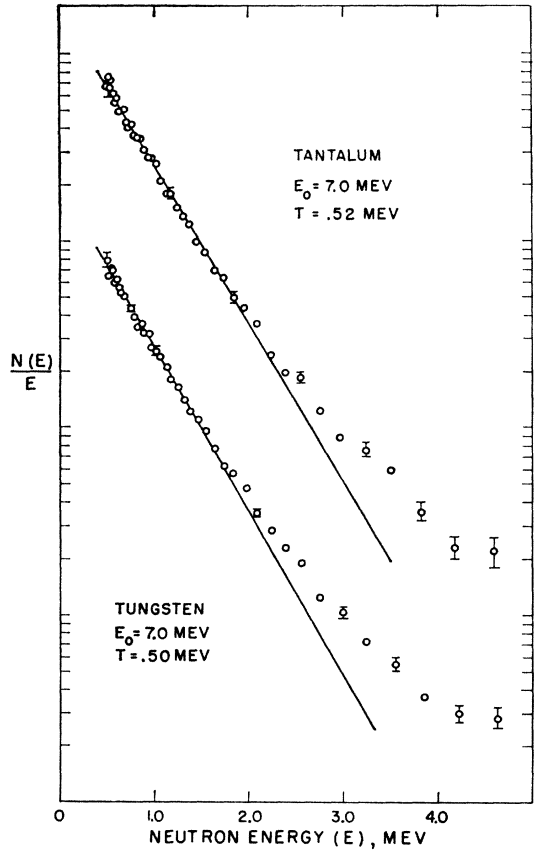

FIG. 9. Plots of $\ln[N(E)/E]$ vs emitted neutron energy (E) for the inelastic scattering of 7.0-MeV neutrons by tantalum and tungsten.

5.0 MeV, of the elastic peak shapes for carbon with the gamma-ray peak from indium. It was concluded that the gamma-ray line shape, for any given run, would give an adequate estimate for the shape of the elastic peak.

An example of the subtraction procedure is shown in Fig. 11. The original time spectrum was plotted on a log scale, and the gamma-ray line shape was plotted on another log sheet. The two plots were superimposed and fitted so that the gamma-ray line was normalized to the height of the peak corresponding to the energy of the elastically scattered neutrons. All of the neutron counts in the normalized curve were assumed to be elastic, and were subtracted. The errors assigned to each point are indicated in Figs. 5 through 10 and 12 through 14. They include a contribution due to an estimated error in the subtraction of the elastic peak. The error in this fitting and subtraction procedure is the dominant one for the points closest to the elastic peak.

The assignment of neutron energy corresponding to a given channel was obtained simply by observing the neutron flight time corresponding to a known flight path. The flight time was obtained by observing the number of channels between the channel in question and the center of the gamma-ray peak, and then adding the flight time of the gamma ray. The time spectrum was corrected for detector sensitivity and converted to an energy spectrum by the relation

$$N(E)=N(t)(dt/dE)=N(t)t/2E. \tag{13}$$

Figure 12 shows a typical plot of $N(E)$ vs E, corresponding to the time spectrum of Fig. 2, for 7.0-MeV neutrons scattered by Cu. Finally, each spectrum was divided by E and plotted in the form of Eq. (4), where all energies have been converted to the center-of-mass system from the original data in the lab system. Figure 6 shows a nuclear temperature plot corresponding to the data in Figs. 2 and 12.

As a test of reproducibility the indium temperature was measured with each series of runs with other elements, at each incident energy. The indium temperature was found to be reproducible to within $\pm 5\%$ over a variety of experimental conditions, such as different flight path, different pulse-beam widths and for several independent calibrations of the detector sensitivity and the time per channel.

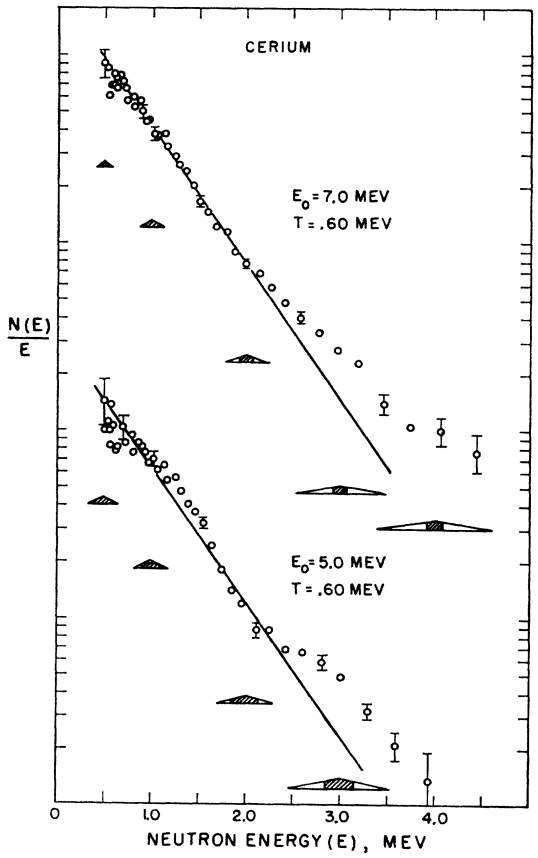

FIG. 10. Plots of $\ln[N(E)/E]$ vs emitted neutron energy (E) for the inelastic scattering of neutrons by cerium at incident energies of 5.0 and 7.0 MeV. The triangles show the resolution functions.

The shapes of the neutron spectra are, of course, influenced by the experimental energy resolution. One resolution limitation stems from the finite time width of the beam pulses, and is given by the width of the gamma-ray peak on each time spectrum. This width is constant over the time spectrum, so that it represents a variable energy width. For most of the temperature plots shown the energy spread corresponding to the time width at half-maximum of the gamma-ray peak is given by the energy spread corresponding to any three, or in some cases four, successive points. This width varies from around one MeV for the highest energy neutrons to less than 100 keV for the lowest neutron energies shown. By folding a representative resolution function into a typical Maxwell-evaporation distribution it was found that the effect of the variable energy resolution on an observed nuclear temperature was negligible. Consideration of Table I shows that in most cases the energy thickness of the target is the dominant resolution limitation at the lower energy portion of the spectra. Typical resolution functions, which include both target thickness and burst duration, are shown in Fig. 10. Though these resolution effects did not appreciably change the gross temperature slopes over the spectra, they naturally have the effect of masking any fine structure which may be present.

Multiple scattering should increase the number of low-energy neutrons observed compared to the true spectra. The effect was investigated experimentally by comparing the spectra obtained for various thicknesses of scatterer. The spectrum from a typical indium sample, which had a transmission of about 90% was compared to that obtained with a sample about one-fourth as thick. Within an uncertainty of about $\pm 5\%$, no difference in temperature was noted at 4.0 MeV, or at 7.0 MeV. Similar results were obtained for iron, and

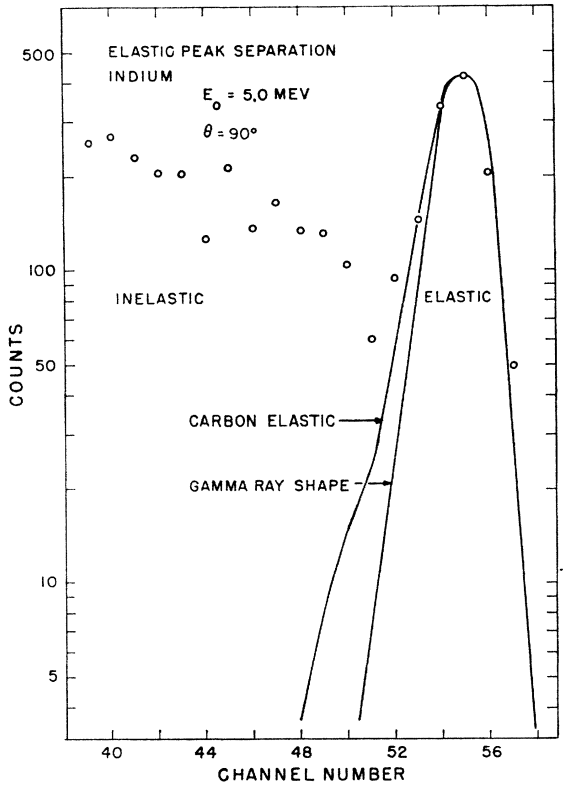

FIG. 11. Typical separation of the elastically and inelastically scattered neutrons.

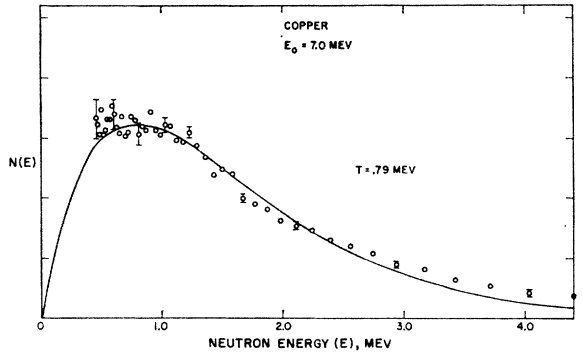

FIG. 12. Plot of $N(E)$ vs emitted neutron energy (E) for the inelastic scattering of 7.0-MeV neutrons by copper.

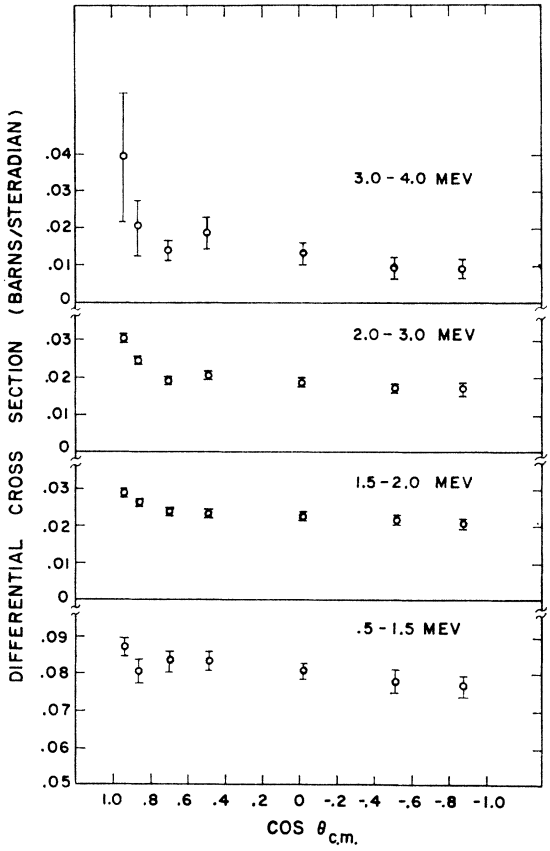

FIG. 13. Angular distributions for the inelastic scattering of 5.0-MeV neutrons by niobium.

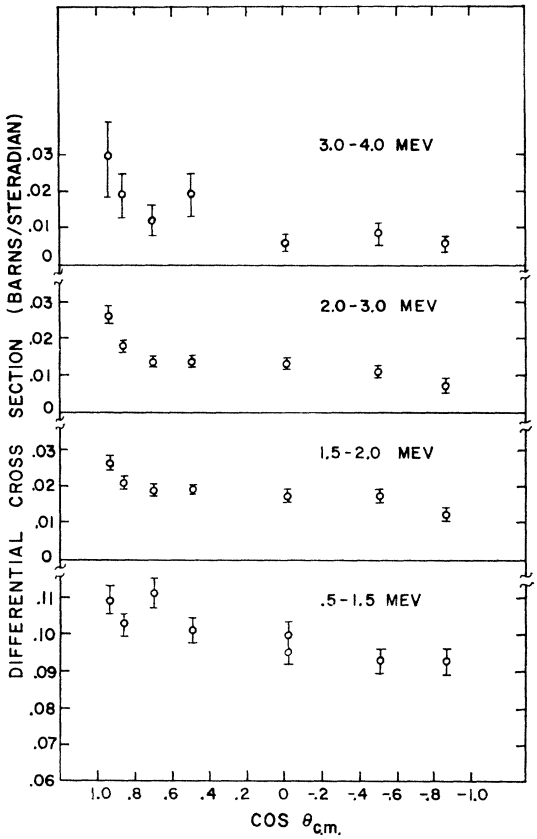

FIG. 14. Angular distributions for the inelastic scattering of 5.0-MeV neutrons by indium.

for copper, at 7.0 MeV. It was concluded that multiple scattering could be neglected for the experimental conditions of these measurements.

A spectrochemical analysis[51] was made for the samples of indium, niobium, and thallium, since these samples best represented the various kinds of results obtained during the course of the work. The most prominent impurity was lead in the thallium sample with an atomic abundance of between 0.1 and 1.0%. All other impurities were much less abundant. The impurities were considered negligible.

D. Cross Sections

The cross sections for inelastic scattering are of interest for comparison with theoretical predictions, and also for calculations involved in reactor shielding problems. Differential cross sections in barns per steradian were obtained by comparison with *n-p* scattering, as in previous work[3,50] for most of the cases for which a nuclear temperature was measured. In the instances where *n-p* comparisons were not obtained the comparison was made with indium since it had been studied thoroughly at each incident energy. The cross-section determinations required corrections for the attenuation of the incident and the scattered beam both for the element measured and for the sample used as a standard. The transmissions of the scattering cylinders usually exceeded 90% so the attenuation corrections were small, and were obtained by a method used in earlier work.[3,45] For these corrections the attenuation of the outgoing beam due to an inelastic scattering process was estimated from the nonelastic cross sections at the average energy ($2T$) on the basis of results compiled by Hughes and Schwartz[52] and by Beyster.[53] The attenuation corrections varied from 2 to 15%, depending on the sample and incident energy, and are thought to be accurate to about ±10% of the correction itself. Table II lists the measured differential cross sections.

The total inelastic cross section is given by

$$4\pi\sigma_{\text{soft}}(90°)+4\pi\sigma_{\text{obs}}(90°).$$

TABLE II. Differential cross sections.

Element	E_0 (MeV)	Inelastic cross section, 90° 0.5 to 3.0 MeV (barns/sr)	3.0 to 5.0 MeV (barns/sr)	Elastic cross section, 90° (barns/sr)
Al	7.0	0.0392±0.004	0.020 ±0.004	0.0298±0.006
V	7.0	0.0736±0.007	0.016 ±0.003	0.0193±0.004
Mn	7.0	0.0729±0.009	0.017 ±0.003	0.0149±0.003
Fe	7.0	0.0753±0.007	0.017 ±0.003	0.0274±0.005
Cu	7.0	0.0857±0.008	0.0155±0.003	0.0414±0.008
Cu	5.0	0.0975±0.013	0.021 ±0.007	0.051 ±0.010
As	7.0	0.0939±0.009	0.021 ±0.004	0.060 ±0.012
Se	7.0	0.0993±0.010	0.0175±0.003	0.0385±0.008
Sr	7.0	0.100 ±0.010	0.0217±0.004	0.047 ±0.009
Nb	7.0	0.0970±0.010	···	0.0475±0.009
Nb	6.0	0.112 ±0.011	0.021 ±0.005	0.052 ±0.010
Nb	5.0	0.111 ±0.011	0.0145±0.004	0.072 ±0.014
Nb	4.0	0.141 ±0.014	···	0.083 ±0.016
In	7.0	0.118 ±0.009	0.0124±0.002	0.023 ±0.005
In	6.0	0.131 ±0.013	0.0145±0.003	0.022 ±0.004
In	5.0	0.125 ±0.010	0.0067±0.002	0.032 ±0.006
In	4.0	0.120 ±0.012	···	0.0365±0.007
Sb	7.0	0.135 ±0.014	···	0.053 ±0.011
Sb	4.0	0.136 ±0.014	···	0.0325±0.0061
I	7.0	0.132 ±0.014	···	0.0445±0.009
I	4.0	0.134 ±0.014	···	0.035 ±0.007
La	7.0	0.127 ±0.015	···	0.102 ±0.020
La	5.0	0.128 ±0.016	0.019 ±0.006	0.032 ±0.006
La	4.0	0.158 ±0.018	···	0.066 ±0.013
Ce	7.0	0.128 ±0.013	0.0175±0.003	0.048 ±0.010
Ce	5.0	0.142 ±0.016	0.019 ±0.006	0.028 ±0.006
Ta	7.0	0.150 ±0.017	0.0114±0.002	0.0565±0.013
W	7.0	0.140 ±0.016	0.0103±0.002	0.0465±0.009
Au	7.0	0.146 ±0.015	···	0.101 ±0.020
Au	4.0	0.172 ±0.017	···	0.155 ±0.031
Tl	7.0	0.147 ±0.015	···	0.110 ±0.022
Tl	6.0	0.158 ±0.016	0.035 ±0.008	0.090 ±0.018
Tl	5.0	0.164 ±0.016	0.023 ±0.007	0.115 ±0.023
Tl	4.0	0.165 ±0.017	···	0.163 ±0.033
Pb^{206}	7.0	0.147 ±0.015	0.0234±0.0033	0.0409±0.0040
Pb^{206}	4.0	0.133 ±0.014	0.0371±0.0037	0.112 ±0.011
Bi	7.0	0.152 ±0.018	0.0217±0.004	0.0835±0.016
Bi	4.0	0.127 ±0.013	···	0.147 ±0.015

[51] Spectrochemical analysis by Joe A. Mariner, Los Alamos spectroscopic group.

[52] D. J. Hughes and R. B. Schwartz, *Neutron Cross Sections* Brookhaven National Laboratory Report BNL-325 (U.S. Government Printing Office, Washington, D. C., 1958), 2nd ed.

[53] J. R. Beyster, Los Alamos Report 2099, 1957.

TABLE III. Extrapolated total inelastic cross sections.

Element	E_0 (MeV)	Total inelastic cross section[a] (barns)	Nonelastic cross section[b] (barns)	References	
Al	7.0	0.81 ±0.08	0.84	53	
Ti	7.0	···	1.29	53	
V	7.0	1.27 ±0.11	···		
Mn	7.0	1.24 ±0.13	···		
Fe	7.0	1.29 ±0.11	1.41	53	
Cu	7.0	1.46 ±0.12	1.60	52	
Cu	5.0	1.74 ±0.22	1.70	52	
As	7.0	1.70 ±0.15	···		
Se	7.0	1.78 ±0.16	1.6	53	
Sr	7.0	1.74 ±0.16	···		
Zr	7.0	···	1.72	53	
Nb	7.0	1.56[c]±0.16	···		
Nb	6.0	2.20 ±0.20	···		
Nb	5.0	2.13 ±0.20	···		
Nb	4.0	2.74[c]±0.34	···		
Mo	7.0	···	1.87	53	
Cd	7.0	···	2.03	52	
In	7.0	2.09 ±0.15	···		
In	6.0	2.39 ±0.22	···		
In	5.0	2.27 ±0.18			
In	4.0	2.35[c]±0.24			
Sn	7.0	···	2.07	52	
Sb	7.0	2.17[c]±0.23	···		
Sb	4.0	2.65[c]±0.28	···		
I	7.0	2.11[c]±0.22	···		
I	4.0	2.54[c]±0.27	···		
Ba	7.0	···	2.17	53	
La	7.0	1.94[c]±0.23	···		
La	5.0	2.19 ±0.26	···		
La	4.0	2.48[c]±0.28	···		
Ce	7.0	2.26 ±0.21	···		
Ce	5.0	2.50 ±0.27	···		
Ta	7.0	2.67 ±0.29	2.50	53	
W	7.0	2.53 ±0.28	2.5	52	
Au	7.0	2.32[c]±0.24	2.50	53	
Au	4.0	3.06[c]±0.30	2.94	53	
Tl	7.0	2.20[c]±0.22	···		
Tl	6.0	2.76 ±0.26	···		
Tl	5.0	2.69 ±0.25	···		
Tl	4.0	2.46[c]±0.25	···		
Pb^{206}[d]	7.0	2.39 ±0.24	2.38–2.62	52	Natural abundance
Bi	7.0	2.41 ±0.26	2.48	53	

[a] The total inelastic cross sections have been obtained from the differential cross sections observed at 90°, Table II. Equation (4) was assumed, at the temperature (T) listed in Table IV, to obtain the total differential inelastic cross section from each observed spectrum. Angular isotropy was assumed to obtain the extrapolated total inelastic cross section.

[b] Nonelastic cross sections obtained by previous experimenters are listed for comparison with the results of the present work. For the incident energies listed, the total inelastic cross sections should be nearly equal to the nonelastic cross sections.

[c] The energy interval above 3.0 MeV was not available from the spectrum on which this observation was based. The extrapolated cross section will therefore be correspondingly low.

[d] The isotope Pb^{206} is 88% abundant.

The σ_{obs} values are listed in Table II. The quantity σ_{soft} represents the differential cross section for those neutrons in the energy interval zero to 0.5 MeV, obtained by extrapolation of Eq. (4). The measured nuclear temperatures (given by Table IV) were used for the extrapolation. Table III shows the resulting total inelastic cross sections. Table III also shows, for comparison, previously measured values for the total nonelastic cross sections for the various elements. Since reactions other than inelastic scattering are usually negligible, the agreement is satisfactory. Similarly, good agreement was obtained for the case of indium where the extrapolated cross sections were added to measured total elastic cross sections and compared with the corresponding total cross section determined independently by transmission measurements.

E. Angular Distributions for In and Nb

Inelastically scattered neutrons were observed at each of six angles for niobium and for indium, at an incident energy of 5.0 MeV. The continuum region was divided into four energy intervals, and the angular distributions corresponding to each of these intervals are given by Figs. 13 and 14.

IV. DISCUSSION OF RESULTS

A. The Observed Continuous Spectra

The usefulness of Eq. (4) for representing the observed spectra of the inelastically scattered neutrons is shown by Fig. 5 through 10. All of the elements except the very lightest ones give good fits at an incident energy (E_0) of 7.0 MeV. For the lower incident energies most of the elements observed also give good fits. In general, the $\ln[N(E)/E]$ vs E plots are linear in the range of 0.5 to 2.0 MeV. Some cases show this linearity extending as high as 3.0 MeV, particularly for elements such as thallium, bismuth, and iron, for which higher temperatures are observed. Table IV lists values for

TABLE IV. Values for the nuclear temperature (T); the level density coefficients (a) and (a') as defined by Eqs. (8), (16), and (17), and the level density coefficients corrected for pairing energy (a_p) and (a_p') obtained from Eqs. (18), (19), and (20), for each nucleus and incident energy of the present work.

Element	E_0 (MeV)	T (MeV)	a (MeV^{-1})	a' (MeV^{-1})	a_p (MeV^{-1})	a_p' (MeV^{-1})
Al	7.0	0.96±0.15	5.5	10.5	3.2	8.7
V	7.0	0.90±0.09	6.4	11.7	4.6	10.1
Mn	7.0	1.00±0.10	5.0	9.8	3.7	8.8
Fe	7.0	0.95±0.06	5.7	10.7	2.6	8.5
Cu	7.0	0.79±0.06	8.7	14.6	6.4	12.4
Cu	5.0	0.72±0.07	6.9	13.5	4.1	11.5
As	7.0	0.67±0.06	12.6	19.3	9.3	16.3
Se	7.0	0.62±0.05	15.0	22.1	8.0	15.7
Sr	7.0	0.80±0.08	8.4	14.2	4.6	11.0
Nb	7.0	0.59±0.03	16.7	24.2	14.9	22.5
Nb	6.0	0.49±0.05	20.9	29.9	18.3	27.4
Nb	5.0	0.48±0.05	17.5	26.2	14.8	24.3
Nb	4.0	0.33±0.03	30.7	44.0	24.9	38.6
In	7.0	0.56±0.02	18.8	26.6	14.6	22.7
In	6.0	0.52±0.03	18.3	26.8	13.6	22.4
In	5.0	0.48±0.04	17.6	26.9	11.9	21.7
In	4.0	0.40±0.03	20.0	31.3	11.9	24.0
Sb	7.0	0.58±0.05	17.4	24.9	13.5	21.3
Sb	4.0	0.40±0.04	20.0	31.3	12.0	24.1
I	7.0	0.60±0.05	16.1	23.5	12.8	20.3
I	4.0	0.41±0.04	18.9	29.9	11.8	23.6
La	7.0	0.68±0.06	12.2	18.8	11.0	17.7
La	5.0	0.69±0.07	7.6	14.5	6.5	13.6
La	4.0	0.65±0.07	6.4	14.0	5.1	13.1
Ce	7.0	0.60±0.06	16.2	23.5	11.3	18.9
Ce	5.0	0.60±0.07	10.6	18.3	5.7	14.3
Ta	7.0	0.52±0.04	22.1	30.4	18.5	27.0
W	7.0	0.50±0.05	24.0	32.6	15.4	24.5
Au	7.0	0.60±0.06	16.1	23.5	14.4	21.9
Au	4.0	0.47±0.04	13.9	23.7	11.1	21.2
Tl	7.0	0.78±0.06	8.9	15.0	8.1	14.0
Tl	6.0	0.80±0.05	6.9	12.8	6.1	12.1
Tl	5.0	0.81±0.05	5.2	11.3	4.4	10.7
Tl	4.0	0.76±0.05	4.3	11.2	3.4	10.7
Bi	7.0	1.05±0.07	4.5	9.1	3.7	8.5
Bi	5.0	0.68±0.09	7.9	14.9	6.1	13.4
Pb^{206}	7.0	0.92±0.09	6.1	11.2	4.5	9.9

all of the nuclear temperatures observed during the course of the work.

The lighter nuclei, aluminum and vanadium, show very definite structure. The aluminum structure shows up most strikingly, as shown by Fig. 5. The semidiscrete structure indicated by the light nuclei such as aluminum and vanadium is to be expected. However, a straight line has been drawn through these distributions to approximate crudely their spectra. There is also an appearance of weakly excited structure for iron, but the fit shown is reasonably good in the low-energy region and continues to 4.0 MeV. Cerium exhibits a typical temperature distribution for the 7.0-MeV incident energy, but shows definite structure at 5.0 MeV.

For the rest of the elements the most important departure from Maxwell-evaporation fits is the appearance of the high-energy neutron excess, mentioned earlier, which corresponds to excitation of the lower lying states. These neutrons, in excess of the linear extrapolation are generally first seen to appear in the spectra for neutron energies (E) of about 2.0 MeV and to increase in number for higher neutron energies. The most pronounced appearances of neutron excess are seen in Fig. 7 for niobium, where at the lower incident energies the excess breaks away from a linear fit [Eq. (4)] very abruptly in E values of about 1.2 to 1.5 MeV. Bismuth, on the other hand, does not show the neutron excess, but shows instead a dearth of high-energy neutrons, which is consistent with a sparsity of low-lying levels. For most of the spectra it appears that the assumptions which lead from Eq. (2) to Eq. (4) are reasonably good in the region of 0.5 to 2.0 MeV, and that the nuclear temperature concept makes possible a useful description of the data. This region contains more than 70% of the observed inelastic neutrons. The persistent appearance of the neutron excess at each of several incident energies suggests, however, that direct interaction processes are in evidence.

B. Investigation of the Effects of Reaction Mechanisms

Detailed data were taken for several elements to obtain information concerning the reaction mechanisms. First, the energy distributions of the inelastically scattered neutrons were observed as a function of angle for indium and niobium at an incident energy of 5.0 MeV. Second, in an effort to determine separately the effects of $S(E^*)$ and $\sigma_i(E,E^*)$ on the continuous spectra, the quantity $\ln[N(E)/E]$ was plotted against E^* for indium for each of the four incident energies used. The separate curves of $\ln[N(E)/E]$ vs E^* were superimposed onto one curve and normalized to get the best possible matching of slopes in the regions of overlapping values of E^*. The justification for this procedure is seen from Eqs. (2) and (3). They show that $\ln[N(E)/E]$ is equal to $\ln \text{ const}(E_0)+S(E^*)+\ln\sigma_1(E,E^*,E_0)$ for any given incident energy E_0. It is seen that the only term which depends on E^* independently of E_0 is $S(E^*)$.

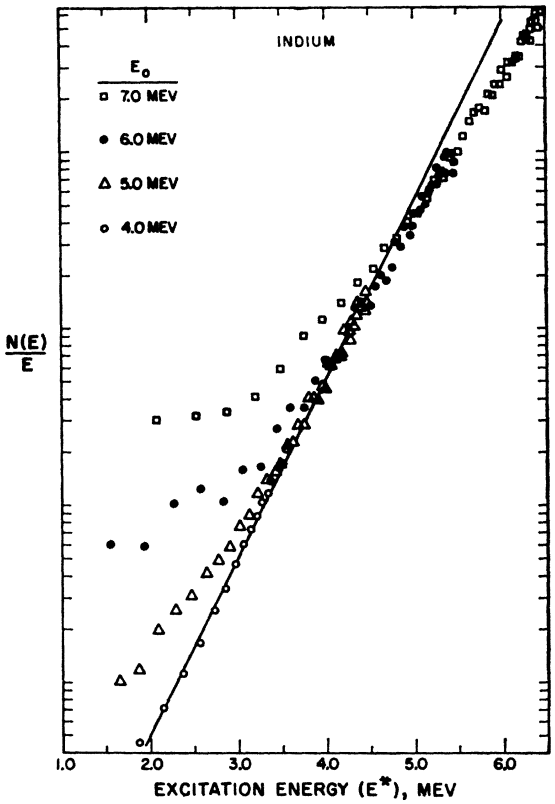

FIG. 15. Plots of $\ln[N(E)/E]$ vs excitation energy (E^*) for neutrons scattered inelastically by indium.

Figure 15 shows an example of this analysis. If the slopes of the curves for different incident energies are dependent solely on $S(E^*)$, then the different curves should each have the same slope at any value of E^* where two or more of the curves overlap. However, if $\sigma_i(E,E^*)$ varies significantly with neutron energy, then the slopes for the different curves will not be the same at any given E^*, and the curves will not overlap. Figure 15 shows that the latter statement describes the situation for those points corresponding to the neutron excess discussed earlier. The neutron excess is clearly seen to be associated with the neutron energies and hence is plausibly interpreted to be caused by the variation of $\sigma_i(E,E^*)$ rather than a fluctuation of $S(E^*)$.

1. Indium

The variation of the indium temperatures with E_0 seen in Table IV suggests that the Fermi gas prediction is valid. Therefore, $\ln[N(E)/E]$ has been plotted against $\sqrt{E^*}$ in a way similar to Fig. 15; and Fig. 16 shows the result. It is seen that there is good overlapping for those portions of each of the four curves corresponding to the lower-energy neutrons and that those points all fall on a common straight line. Com-

parison of Fig. 15 and Fig. 16 indicates that the present data, plotted over the energy range shown, can distinguish between $S(E^*) \propto E^*$ and $S(E^*) \propto \sqrt{E^*}$. For indium, the $\sqrt{E^*}$ dependence is seen to give the better over-all fit in agreement with Fermi-gas predictions. This result for indium is shown quantitatively by the constancy of the values of a as a function of E_0 as given in Table IV.

Now consider the indium angular distributions of Fig. 14, taken at an incident energy of 5.0 MeV. The neutrons in the energy intervals 2.0 to 3.0 MeV and 3.0 to 4.0 MeV show a definite tendency toward forward peaking. As shown by Figs. 14 and 15, the 2.0- to 4.0-MeV neutrons are the ones which show the largest effect. Thus, if one associates the forward peaking of the angular distributions with direct interactions, it appears that the neutron excess is caused primarily by direct interactions. For indium the level density of the compound nucleus at the neutron binding energy is of the order of ten levels per 100 eV, as indicated by slow-neutron resonance data.[52] If the value of a (19 per MeV) from Fig. 16 is used with Eq. (9) it is predicted that more than 10^6 compound-nucleus levels for $l=0$ alone may be excited by the 5.0-MeV incident beam, which had an energy spread of 288 keV (Table I). If this many compound-nucleus levels are excited, it seems plausible that the statistical assumption would be valid and there would presumably be no asymmetries caused by residual interference between CN states. This consideration gives support to the assumption that direct interaction is the cause of the asymmetries observed in Fig. 14. Figures 14 and 16 illustrate the point[54] that for inelastic neutron scattering, a favorable way to observe direct interaction of a given level, or group of levels, is to use an incident beam of sufficient energy that most of the compound-nucleus decay goes to the higher E^* values. This statement is consistent with the results obtained earlier for magnesium[55–57] and with the conclusions of Rosen and Stewart.[30]

It is of interest to note that Fig. 14 appears to show a slight amount of forward peaking for the low-energy neutrons as well, though percentage-wise it is much less significant than for the higher energies. By taking the average differential cross section for the points at 90°, 120°, and 150°, and multiplying by 4π, one can separate the isotropic components from the forward-peaked components of the total inelastic cross section, for each of the energy intervals shown in Fig. 14. By calculating σ_{soft}, assuming that it is isotropic, and including it in the total, it turns out that for this case only 4% of the inelastic cross section is forward-peaked. This fact is

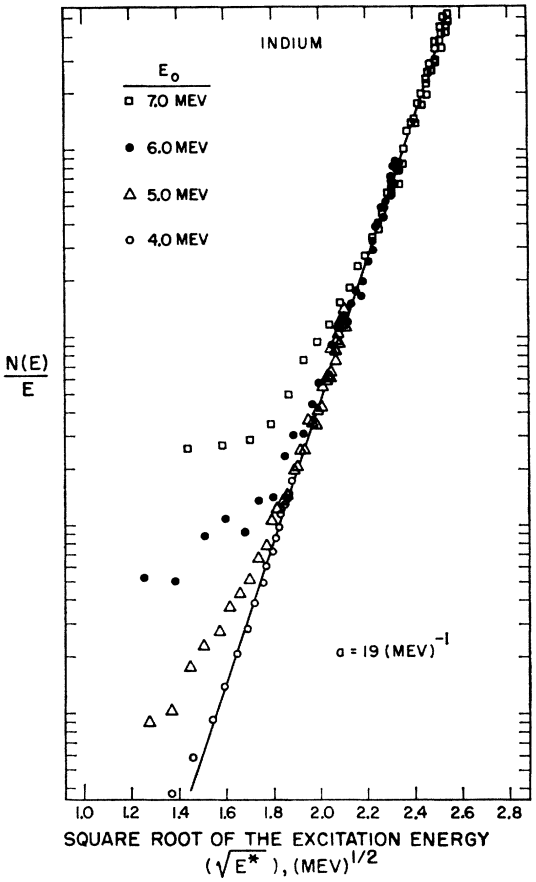

FIG. 16. Plots of $\ln[N(E)/E]$ vs the square root of the excitation energy ($\sqrt{E^*}$) for neutrons scattered inelastically by indium.

consistent with a predominance of the compound-nucleus processes.

To obtain a quantitative description of how $\sigma_i(E,E^*)$ varies with energy, the level density for indium has been assumed to follow the straight line drawn in Fig. 16, namely, the form of Eq. (9), with $a=19$/MeV. Then by Eq. (2) a plot of $N(E)/E \exp[2(19E^*)^{1/2}]$ vs E^* gives the energy dependence of $\sigma_i(E,E^*)$. Figure 17 shows plots of this form for indium for each of the incident energies. For each E_0, the quantity $N(E)/E \times \exp[2(19E^*)^{1/2}]$ has been normalized to unity in the region of low E. This is the region where the data are most accurate and where compound-nucleus production is believed to predominate.

Figure 17 illustrates the constancy and then rapid increase in $\sigma_i(E,E^*)$ as one proceeds from high to lower-lying levels for a given value of E_0. The values of $N(E)/E \exp[2(19E^*)^{1/2}]$ normalized as shown in Fig. 17, are equivalent to a ratio of the form [$\sigma_i(E,E^*) \neq$ constant with energy]/[$\sigma_i(E,E^*)$ = constant with energy]. These ratios may be used to separate the neutron counts associated with processes for which $\sigma_i(E,E^*) = \text{const}$ (presumably CN) from those of processes for which $\sigma_i(E,E^*) \neq \text{const}$ (presumably DI), in the original time

[54] V. F. Weisskopf, Rev. Mod. Phys. **29**, 174 (1957).
[55] D. B. Thomson, L. Cranberg, and J. S. Levin, Bull. Am. Phys. Soc. **3**, No. 7, Paper G-9 (1958).
[56] D. B. Thomson, L. Cranberg, and J. S. Levin, Phys. Rev. **125**, 2049 (1962).
[57] R. L. Clark and W. G. Cross, Bull. Am. Phys. Soc. **4**, No. 4, Paper NA-11 (1959).

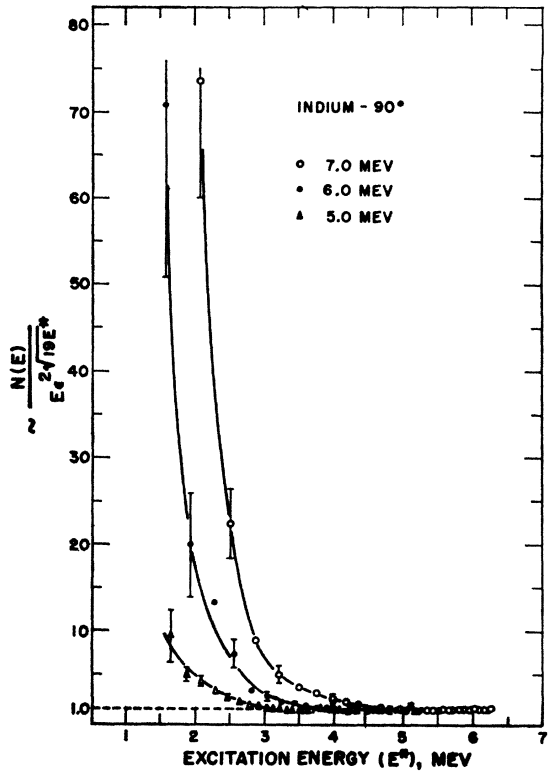

FIG. 17. The energy dependencies of the inverse cross section for indium.

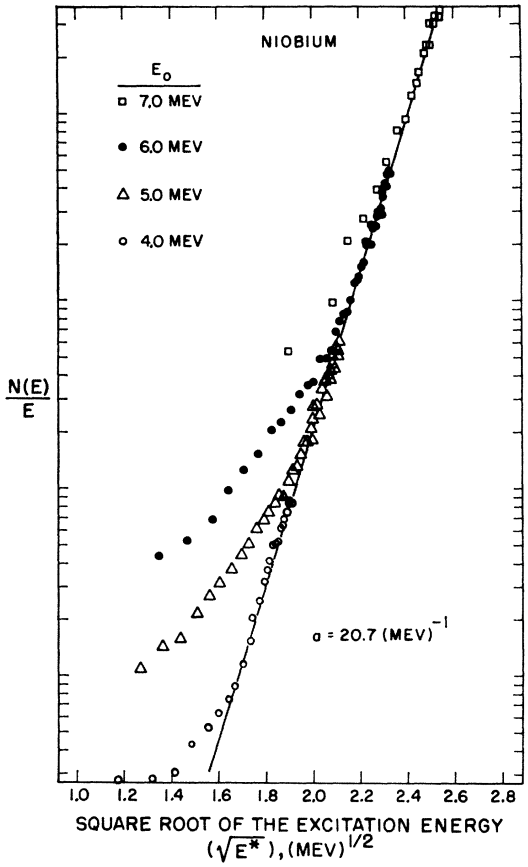

FIG. 18. Plots of $\ln[N(E)/E]$ vs the square root of the excitation energy ($\sqrt{E^*}$) for neutrons scattered inelastically by niobium.

spectra of the inelastically scattered neutrons. This procedure enables one to estimate the percentages of the (n,n') cross section due to the two processes, and the result for indium at 5.0 MeV at 90° is that 7.5% of the cross section is due to the $\sigma_i(E,E^*)\neq$const process.

The 7.5% value, when compared with the 4% value for the forward peaking in the angular distributions of Fig. 14, might indicate that a substantial number of reactions for which $\sigma_i(E,E^*)\neq$const do not give forward peaking. Substantiation of this conclusion would require observations leading to Fig. 17, taken as a function of angle.

A similar calculation, for indium at 7.0 MeV at 90°, again based on Fig. 17, gives a value of 9% of the (n,n') cross section due to the $\sigma_i(E,E^*)\neq$const process.

A result similar to that of Fig. 17 would be obtained if one had instead assumed $W(E^*)$ for indium to follow the form of Eq. (14), Fig. 22.

2. *Niobium*

In the same manner as for indium, the niobium spectra were plotted in the form $\ln[N(E)/E]$ vs $\sqrt{E^*}$, as shown in Fig. 18. Again we interpret the neutron excess as being due to the direct-interaction part of the inverse cross section, and note that it is even more pronounced than it was for indium. In particular, the prominent departures from the Maxwellian fits of Fig. 7 are clearly shown to be a function of the incident neutron energies and hence are presumed to be due to $\sigma_i(E,E^*)$. The angular distributions taken at 5 MeV for niobium, are shown by Fig. 13. The results are very similar to those for indium, with the forward peaking increasing for the higher energy neutrons. By an analysis similar to that used for indium, it was found that 7% of the total inelastic cross section is forward-peaked. As far as reaction mechanisms are concerned the remarks made for indium apply to niobium with perhaps an even greater effect due to direct interactions.

3. *Thallium, Lanthanum, and Copper*

For thallium, plots of $\ln[N(E)/E]$ vs E^* are given in Fig. 19. The neutron excess shows up only slightly. It appears that the direct-interaction contribution is substantially smaller than for indium and niobium, and that with thallium the assumption of energy invariance for the inverse cross section appears to be more accurate than for many of the other nuclei. Figure 20 shows a similar plot for lanthanum. There appears to be substantial evidence for direct-interaction excitation of

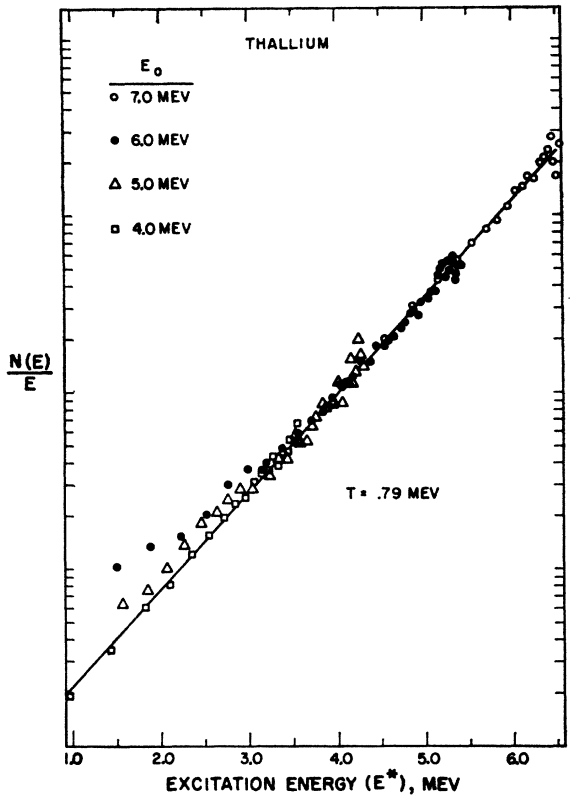

FIG. 19. Plots of $\ln[N(E)/E]$ vs excitation energy (E^*) for neutrons scattered inelastically by thallium.

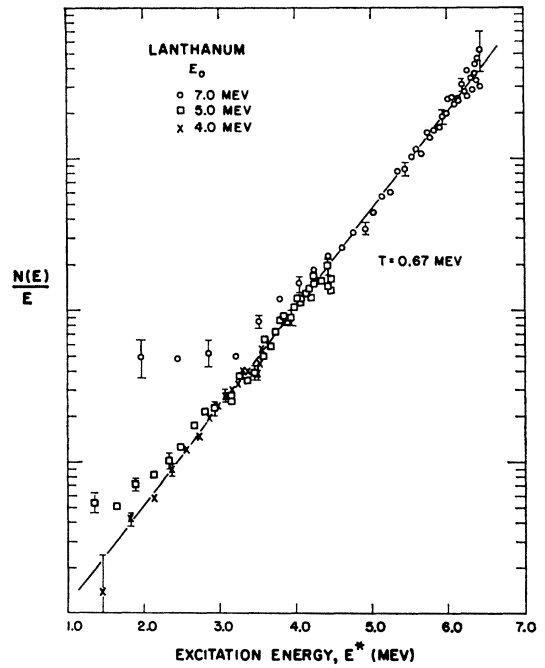

FIG. 20. Plots of $\ln[N(E)/E]$ vs excitation energy (E^*) for neutrons scattered inelastically by lanthanum.

levels below 3 MeV for the 7.0-MeV incident beam, as indicated by the neutron excess for this case.

Only two incident energies were studied for copper, but the $\ln[N(E)/E]$ vs E^* overlap plot given in Fig. 21 shows that the inverse cross section definitely gives some neutron excess in the overlapping E^* range of 2.0 to 4.0 MeV, and it seems that a neutron excess is also present for lower values of E^*. At least in the 2.0- to 4.0-MeV region there appears to be significantly less neutron excess than for indium and niobium but more neutron excess than for thallium.

Thus it appears from Figs. 13 through 21 that direct-interaction excitation of the lower lying levels are observed although compound-nucleus effects dominate.

C. The Variation of Level Density with Excitation Energy

Figures 16 and 19 are typical of the different kinds of level density variation observed in this work. As mentioned previously the indium data are better fitted by the Fermi-gas prediction $S(E^*)=2(aE^*)^{\frac{1}{2}}+\text{const}$ than by a constant temperature. The constant a can be obtained from the slope and for Fig. 16 is 19 per MeV. Figure 18 for niobium appears to show $S(E^*)\propto\sqrt{E^*}+\text{const}$ but there are some fluctuations in the slope, particularly below $E^*=3.6$ MeV. Because of the considerable effect ascribed to the reaction mechanism more overlap data would be necessary to determine $S(E^*)$ accurately for niobium below $E^*=4.0$ MeV.

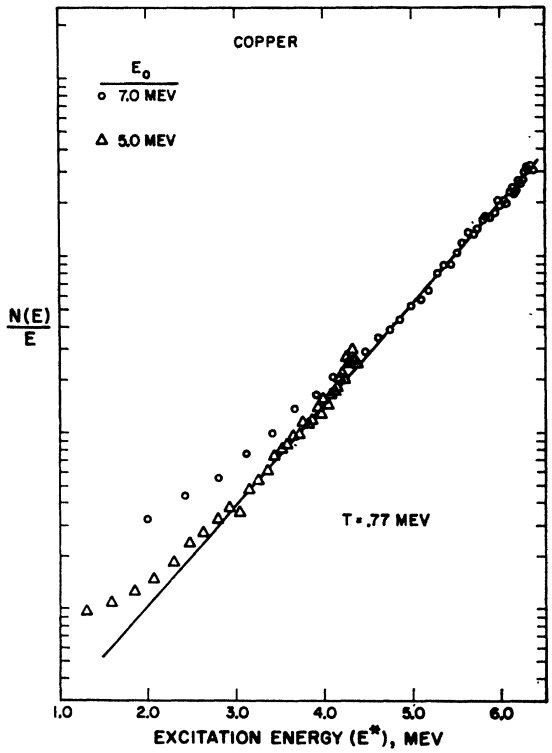

FIG. 21. Plots of $\ln[N(E)/E]$ vs excitation energy (E^*) for neutrons scattered inelastically by copper.

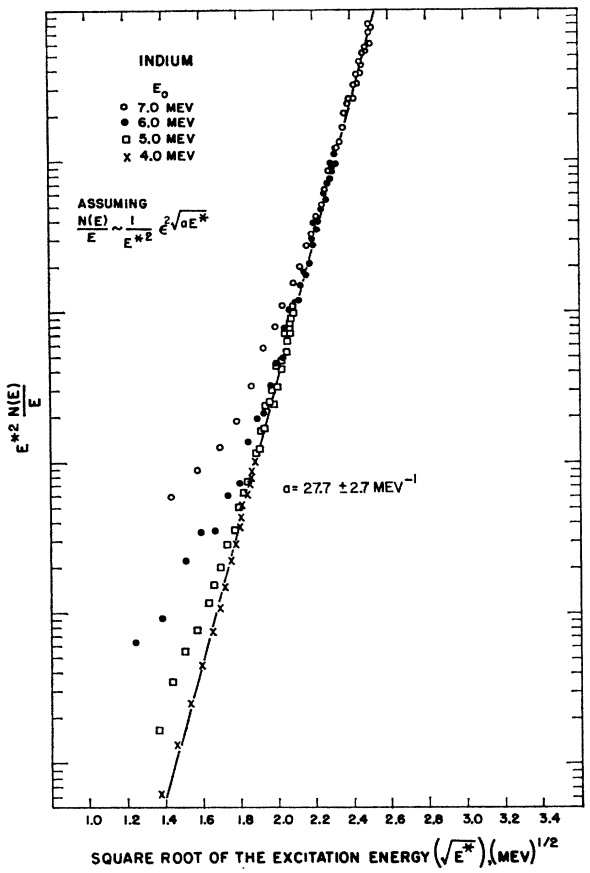

FIG. 22. Plots of $\ln(E^{*2})N(E)/E$ vs the square root of the excitation energy ($\sqrt{E^*}$) for neutrons scattered inelastically by indium at incident energies of 4.0, 5.0, 6.0, and 7.0 MeV. The separate plots of $\ln(E^{*2})N(E)/E$ obtained for each incident energy have been normalized together in regions of overlapping E^*.

Figure 19 for thallium indicates the variation of $S(E^*)$, since the same slope is obtained for each incident energy and for the widest ranges of overlapping values of E^*. For thallium, $S(E^*)=E^*/T+\text{const}$, where $T=0.79\pm0.04$ MeV. The linear variation of $S(E^*)$ with E^* means that the level density is increasing much more rapidly than that of a Fermi gas. Such behavior has been described[26,27,58] in terms of a second-order phase transition or a "melting" of nuclear matter. Figure 20, for lanthanum, shows a similarity with thallium. A linear energy dependence is shown for $S(E^*)$, but more effect of direct interaction is indicated. Figure 21 for copper indicates that $S(E^*)$ may vary more rapidly than $\sqrt{E^*}$, but not quite as rapidly as E^*.

The other cases given in Table IV for which continuous spectra were observed at more than one incident energy were gold, iodine, antimony, cerium, and bismuth. The variation of the observed temperatures with incident energy, indicates that $S(E^*)\propto\sqrt{E^*}$ +const for iodine and antimony, and that $S(E^*)\propto E^*$ +const for cerium. The cerium spectrum Fig. 10, shows significant structure at 5.0 MeV, however, indicating a possible level density fluctuation or a striking effect of the inverse cross section. Finally for bismuth, it appears that the entropy varies less rapidly with excitation energy than a square-root dependence.

It has been pointed out[59] that a more rigorous treatment of the nuclear Fermi-gas model gives a level density expression of the form

$$W(E^*)=(\text{const}/E^{*2})\exp[2(a'E^*)^{1/2}]. \quad (14)$$

A test of this expression for indium is a plot of $\ln[E^{*2}N(E)/E]$ vs $\sqrt{E^*}$, shown by Fig. 22. This form appears to fit the data equally as well as does Fig. 16, and comparison of the two figures indicates that the data are not yet sufficiently accurate to distinguish between Eqs. (9) and (14). These data do indicate, however, that one can distinguish between the forms of Eqs. (9) or (10) on the one hand and a level density formula of the form

$$W(E^*)=\text{const}\exp(E^*/T), \quad (15)$$

where $T=$const, corresponding to $S(E^*)\propto E^*+$const.

Various forms of Eq. (10) have been given,[14,24,58,60] but in view of the fact that we observe cases which are consistent with such diverse forms as Eqs. (9) and (15), corresponding to the simple Fermi gas and to nuclear melting, respectively, it would seem premature to try to distinguish various forms of $f(E^*)$, Eq. (10), from the present data. As the accuracy of the (n,n') and other data improve, however, it should become possible to make such distinctions.

D. Variations of Level Density Coefficients with Mass Number and with Incident Energy

It is of particular interest to study systematic variations of the results in terms of Fermi-gas level density coefficients, such as a, or a', as defined by Eqs. (9) and (14), respectively. We obtain a value of a, or a' from a temperature value by using

$$E_{av}{}^*=E_0-2T, \quad (16)$$

as the average excitation energy corresponding to the spectrum for which the incident energy (E_0) is fixed and the temperature (T) has been determined. Values for a are then obtained from Eqs. (16) and (8). Values of a', corresponding to Eq. (14), may be obtained by use of the formula

$$a'=E^*(1/T+2/E^*)^2, \quad (17)$$

where one again uses (16) for E^*.

Calculation of a and a' values also makes possible a

[58] T. Ericson, Nucl. Phys. 11, 481 (1959).

[59] T. Ericson, in *Proceedings of the International Conference on Nuclear Structure, Kingston, Canada 1960*, edited by D. A. Bromley and E. Vogt (University of Toronto Press, Toronto, Canada, 1960), pp. 697–705.

[60] A. G. W. Cameron, Can. J. Phys. 36, 1040 (1958).

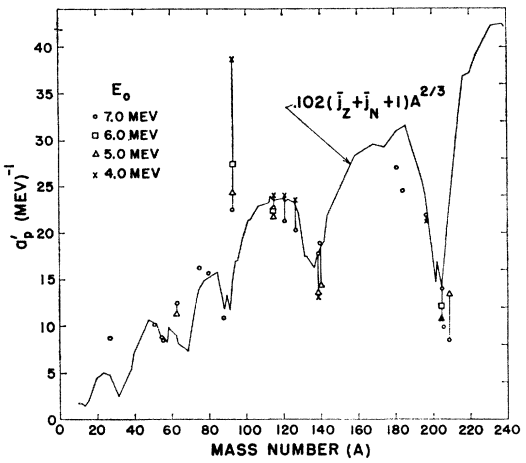

FIG. 23. The corrected level density coefficient a_p', defined by Eqs. (19) and (20) to account for Cameron's[59] pairing energy corrections, plotted vs mass number for each nucleus and incident energy observed during this work. The solid curve is a plot of Eq. (21) using Newton's[24] values for $\bar{j}_Z$ and $\bar{j}_N$.

test of the Fermi-gas prediction that they are independent of E_0 and proportional to the mass number. Table IV lists the values of a and a', defined by Eqs. (8) and (17), respectively, obtained in the present work.

1. *Correlations with Shell-Model Predictions*

At 7.0 MeV, the average value of a given in Table IV is $A/10.9$, and the average value of a' is $A/7.22$. Examination of Table IV shows immediately that there are departures from the Fermi-gas prediction that a, or a', increase linearly with A. Table IV shows very significant correlations with Newton's[24] predictions for the single-particle level density constant "G," Eq. (11). Newton observed striking dips in the level density in the neighborhood of mass numbers 206, 136, 88, 70, and less striking dips at lower mass numbers. Figure 23 shows a curve for a_p' which is similar to Newton's (Reference 24, Fig. 5) which will be discussed later. The predominant dips at mass numbers 206 and 136 correspond closely to doubly magic nuclei, and the dips at the lower A values correspond to singly or doubly magic values. As seen in Table IV, the a and a' values obtained from the present work show dips for bismuth, thallium, cerium, lanthanum, and strontium. The A values for these nuclei correspond to the three most pronounced dips in Newton's curve. It thus appears that the values of the level density coefficients a, and a', and the corresponding nuclear temperatures, are greatly affected by shell structure.

A second effect which appears to be related to the shell structure of an element is the linear energy dependence of the entropy discussed in the previous section. Of the nuclei for which data were taken at more than one value of incident energy, Table IV shows that a and a' increase for thallium, cerium, and lanthanum in accordance with a linear energy dependence for the entropy, i.e., the melting of nuclear matter mentioned earlier. For indium, antimony, and iodine, a and a' appear to be more nearly insensitive to incident energy in agreement with Fermi-gas behavior.

2. *The Effect of Pairing Energy*

We now define level density coefficients, a_p and a_p', based on Newton's excitation energy U, namely

$$U=E_0-2T+P(Z)+P(N), \tag{18}$$

where U is the excitation of the nucleus left over after the removal of the binding energy of pairing. $P(Z)$ and $P(N)$ are the pairing energy corrections for the protons and neutrons, respectively, and are negative.

We may then write

$$a_p=U/T^2, \tag{19}$$

and

$$a_p'=U(1/T+2/U)^2, \tag{20}$$

corresponding to Eqs. (8) and (17).

The temperature data of Table IV have been used with Eqs. (18), (19), and (20) to obtain values of a_p and a_p' for each nucleus and incident energy studied. Cameron's[59] values have been used for $P(Z)$ and $P(N)$, and the results are given in Table IV. The a_p' values are plotted in Fig. 23. The a_p and a_p' values are similar to those for a and a' except, of course, that the a_p values are all lower.

A comparison of the lanthanum and cerium values is particularly interesting. These two nuclei, at mass numbers 139 and 140, respectively, differ only by the addition of an extra proton for cerium which pairs off with the last odd proton of lanthanum. Cameron[60] gives -1.21 MeV for $P(Z)$ for cerium, and zero for lanthanum. The result is that the lanthanum and cerium values for a_p and a_p' shown by Table IV, and Fig. 23, become nearly equal to each other for each value of incident energy as one might expect. These data are too sparse, however, to warrant any general conclusions about the role of pairing energy in this work.

The experimentally determined a_p' values, shown by Fig. 23, were fitted to a Newton curve obtained from the expression $(\bar{j}_Z+\bar{j}_N+1)A^{2/3}$ suggested by Eq. (11). Values listed by Newton[24] were used for $\bar{j}_Z$ and $\bar{j}_N$. The function $(j_Z+j_N+1)A^{2/3}$ was calculated for each nucleus studied in the present work, and compared to the correspondingly observed a_p' values. The resulting experimental fit for the values obtained at 7.0 MeV is the expression

$$a_p'=0.102(\bar{j}_Z+\bar{j}_N+1)A^{2/3}. \tag{21}$$

This equation was then used to evaluate a_p' values for a sufficient number of the more abundant isotopes in the periodic table to give the curve shown by Fig. 23. The curve shows essentially the same dips and plateaus as does Newton's figure (reference 24, Fig. 5). The experimental values for a_p' indicate a correlation with these dips and plateaus.

From both Table IV and Fig. 23 it appears that apart from the pronounced shell-effect dips, the level density coefficients increase with A roughly as predicted by the Fermi-gas model. Equation (21) appears to fit the data shown in Fig. 23 about as well as Newton's original equation fit the slow-neutron data.

Comparison of Eq. (21) with the experimental values in Fig. 23 is complicated by the fact that the value used for each pairing energy applies only to an excitation energy equal to the binding energy of the nucleus in question, and does not necessarily apply to the average excitation energy of the observed spectrum. Cameron[61] has pointed out that the pairing energy is not a constant, but may be a function of excitation energy. Therefore, one does not expect the values used here to apply precisely to these spectra.

It should be kept in mind that use of the expressions (8), (17), (19), and (20) to characterize the data is not consistent for elements such as thallium, which appear to have a linear entropy dependence. However, evaluation of a and a' values is useful as a first step in the systematic comparison of the results for all of the elements.

3. *Comparison with Results of Previous Experiments*

Table V lists available values of nuclear temperatures obtained by inelastic neutron scattering in previous experiments for elements used in the present work. Table V includes corresponding values for the level density coefficient, a', as defined by Eq. (17). Some of the results shown have been corrected for second-particle emission, as indicated. No correction was necessary when the incident energy was 7 MeV or less. Tables IV and V facilitate a comparison of the present results with the earlier work.

It is particularly interesting to consider Ericson's[58] analysis of reaction and scattering data for several light elements. He has used a method of counting the individual levels to obtain the level density as a function of excitation energy. For isotopes of iron and manganese, he concludes that $S(E^*)=E^*/T$ for E^* values of 2 to 6 MeV, or higher. For these two elements, he gets temperatures of 1.15 to 1.2 MeV, which compare with the values of 0.95 to 1.00 MeV obtained from the present work. Ericson concludes that the temperature is nearly constant up to excitations of 10 MeV.

From Tables IV and V the general conclusion emerges that one may find instances both of Fermi-gas behavior and of nuclear melting and that non-Fermi-gas behavior may extend to energies about 10 MeV. However, the work of Cohen and Rubin[8] for iron, copper, and other light elements, together with the increase in a' with E_{av}^* towards the Fermi-gas values observed near closed shells in the present work are consistent with the view that for any given element the Fermi-gas description will become valid if one proceeds to high enough E^*. This is in agreement with the general conclusion of LeCouteur and Lang[14] whose summary includes much high-energy data, and with conclusions of Ericson.[58]

TABLE V. Nuclear temperature and level density coefficient values obtained from inelastic neutron scattering by other experimenters for the elements studied in the present work. The quantity a' is defined by Eq. (17).

Element	Incident energy (E_0) (MeV)	Temperature (T) (MeV)	(a') (MeV^{-1})	Reference
Al	14	0.71±0.10	30.9	1
Al	14	1.06	14.7	2
Mn^{55}	14	1.08±0.09	14.2	67
Fe	14	0.78±0.08[a]	25.9	66
Fe	7.0	0.74±0.074	16.2	65
Fe	5.0	0.85±0.088	10.5	65
Cu	14	0.90±0.09[a]	19.8	66
Cu	14	0.82	23.6	2
Sb	4.1	0.44±0.04	27.0	64
I	14	0.81±0.08	24.1	67
Ta	14	0.95±0.095[a]	17.9	30
Ta	7.0	0.49±0.05	33.9	65
Ta	6.34	0.50±0.05	30.1	4
Ta	5.0	0.50±0.05	25.0	65
Ta	3.40	0.39±0.04	29.0	4
Ta	2.45	0.32±0.03	32.4	4
Ta	2.44	0.37±0.04	25.6	65
W	7.0	0.57±0.06	25.7	65
W	6.34	0.44±0.044	38.0	4
W	5.0	0.55±0.055	21.2	65
W	3.40	0.36±0.036	33.3	4
W	2.45	0.36±0.036	26.8	4
W	2.44	0.38±0.04	24.5	65
Au	14	0.64±0.10	37.6	1
Au	6.34	0.65±0.065	18.9	4
Au	3.40	0.45±0.045	22.8	4
Au	2.45	0.30±0.03	36.0	4
Bi	14	1.05±0.10[a]	14.9	30
Bi	14	0.95±0.09	17.9	67

[a] Corrected for $(n,2n)$ assuming T goes as $\sqrt{E^*}$.

Sherr and Brady's[62] value of 1.5 MeV for the temperature of Fe^{56} by (p,n) and (p,p') measurements, when compared with the results for iron of the present work and of Ericson,[58] leads them to suggest that the discrepancy may be due to the lack of more precise information as to the variation with energy of the inverse cross section. The importance of this variation is borne out by the "overlap" plots discussed in Sec. IV-B.

In a recent paper, Lang[63] has obtained a value of 0.0748 from analysis of the slow-neutron data for the numerical constant of Eq. (21). This compares with the value of 0.102 found in the present work. This disagreement may be due to difference in method of analysis, choice of elements, and excitation energies involved.

[61] A. G. W. Cameron (private communication).

[62] R. Sherr and F. P. Brady, Phys. Rev. **124**, 1928 (1961).
[63] D. W. Lang, Nucl. Phys. **26**, 434 (1961).
[64] L. D. Vincent, R. N. Little, Jr., I. L. Morgan, and J. T. Prud'homme, Bull. Am. Phys. Soc. **5**, No. 2, Paper G-6 (1960).
[65] R. Ewing (private communication).
[66] L. Rosen and L. Stewart, Los Alamos Report 1560, 1953 (unpublished).
[67] R. T. Arnold and G. B. Bunyard, Bull. Am. Phys. Soc. **5**, No. 2, G-7 (1960).

V. CONCLUSIONS

The results of this study have indicated the following general conclusions:

(1). The description of the spectra of inelastically scattered neutrons in terms of nuclear temperature is quite generally useful for medium and heavy-weight nuclei at excitation energies of two or three MeV and higher.

(2). The angular distributions and overlapping E^* plots of $\ln[N(E)/E]$ indicate that compound-nucleus formation occurs for at least 80 to 90% of the inelastically scattered neutrons for incident beam energies in the range of 4.0 to 7.0 MeV. These data also seem to indicate that direct interaction plays a significant role for those neutrons which lose a small amount of energy and momentum in the scattering process.

(3). The observed variations of level density with excitation energy indicate that in the range of several MeV there are nuclei which appear to obey the Fermi-gas prediction that the entropy varies as $\sqrt{E^*}$, other nuclei for which the entropy varies as E^*, and intermediate cases. The observed variations of level density with mass number indicate that the level density decreases significantly for nuclei with mass numbers near closed shell values, such as lanthanum, thallium, and lead in agreement with slow-neutron data. For mass numbers between closed shell values, there is agreement with the prediction that the level density increases with mass number. These results are in fair quantitative agreement with level spacings obtained by the slow-neutron resonance method. In general, the systematic variations discussed by Newton are confirmed.

(4). The method of plotting $\ln[N(E)/E]$ vs E^*, $\sqrt{E^*}$, etc., for measurements of overlapping excitation energies, shows promise of providing a means of separately observing the reaction mechanism effects so that the true level density variations can be obtained from the observed spectra, particularly if these measurements are made with more accuracy and at more incident energies.

ACKNOWLEDGMENTS

The author is greatly indebted to Dr. Lawrence Cranberg for his support throughout the entire course of this work. His active participation and many helpful suggestions facilitated continual improvements of the experimental techniques, aided the interpretation of results, and were invaluable during the writing of this paper.

The author also greatly appreciates the support of Professor L. W. Seagondollar of the University of Kansas in helping make this program possible, his assistance in taking some of the data, and his many helpful discussions. Finally, the author expresses gratitude to Dr. Joseph L. McKibben and members of the staff of the Los Alamos large Van de Graaff accelerator for helping make these experiments possible.